JOURNAL OF GEOPHYSICAL RESEARCH, VOL. 99, NO. B10, PAGES 19,617–19,634, OCTOBER 10, 1994

On the derivation of coseismic displacement fields using differential radar interferometry: The Landers earthquake

Howard A. Zebker, Paul A. Rosen, Richard M. Goldstein,
Andrew Gabriel, and Charles L. Werner
Jet Propulsion Laboratory, California Institute of Technology, Pasadena

Abstract. We present a map of the coseismic displacement field resulting from the Landers, California, June 28, 1992, earthquake derived using data acquired from an orbiting high-resolution radar system. We achieve results more accurate than previous space studies and similar in accuracy to those obtained by conventional field survey techniques. Data from the ERS 1 synthetic aperture radar instrument acquired in April, July, and August 1992 are used to generate a high-resolution, wide area map of the displacements. The data represent the motion in the direction of the radar line of sight to centimeter level precision of each 30-m resolution element in a 113 km by 90 km image. Our coseismic displacement contour map gives a lobed pattern consistent with theoretical models of the displacement field from the earthquake. Fine structure observed as displacement tiling in regions several kilometers from the fault appears to be the result of local surface fracturing. Comparison of these data with Global Positioning System and electronic distance measurement survey data yield a correlation of 0.96; thus the radar measurements are a means to extend the point measurements acquired by traditional techniques to an area map format. The technique we use is (1) more automatic, (2) more precise, and (3) better validated than previous similar applications of differential radar interferometry. Since we require only remotely sensed satellite data with no additional requirements for ancillary information, the technique is well suited for global seismic monitoring and analysis.

Introduction

Interferometric radar techniques for the generation of highly accurate digital elevation models (DEMs) by now have been well documented in the literature [*Zebker and Goldstein*, 1986; *Goldstein et al.*, 1988; *Prati et al.*, 1990; *Zebker et al.*, 1992; *Evans et al.*, 1992; *Madsen et al.*, 1993, also personal communication, 1993; H. A. Zebker et al., personal communication, 1993]. A related application of such techniques allows the measurement of the motion of all resolved points in a remotely sensed image [*Goldstein and Zebker*, 1987; *Goldstein et al.*, 1989]. These similar techniques both follow from analysis and interpretation of interferograms, which consist of the phase differences between two radar images of the same scene acquired at separate locations or times: a sensor location change gives sensitivity to topography and a sensor temporal change gives motion sensitivity. A combination of the two approaches, denoted differential radar interferometry since the phase measurements of interest result from the difference of two interferograms, has previously been used by *Gabriel et al.* [1989] to map the changes in surface elevation of agricultural fields over a large area to centimeter-level sensitivities.

More recently, there has been activity by at least two groups applying the capabilities of radar interferometry to the study of seismic phenomena. *Massonet et al.* [1993] of Centre National d'Etudes Spatiales (CNES) in Toulouse, France, used an interferometric digital elevation model derived from the European Space Agency (ESA) ERS 1 satellite data for analysis of the magnitude 7.3 earthquake centered near Landers, California, on June 28, 1992. In this study a single interferogram which contained phase signals from the local topography and from the earthquake displacements was subtracted from a manipulated U.S. Geological Survey (USGS) 15 arc min DEM of the area. The residual phases were interpreted as ground displacements from the event. The interferogram, when corrected for topographic effects, shows a displaced dual-lobed pattern of fringes emanating from the fault zone, where each fringe represents about 2.8 cm of motion in the radar line of sight direction. They also derive a theoretical fringe pattern from a model of the earthquake motion which matches the observations fairly closely.

Despite its success, there are several important limitations in the technique used for the above study. Although a USGS 90-m spacing DEM was available for this site, for many sites in the world, no DEM exists. In addition, an existing DEM may not be sufficiently accurate to yield the desired precision. DEMs typically contain errors and distortions of the order of the phenomena being investigated. The CNES team estimates a precision in their measurements of about 2.8 cm in the radar line of sight motion, limited mainly by imprecision in the USGS DEM plus radar system noise. Also, the DEM must be precisely coregistered to the radar image, which itself may be a difficult task. (S. N. Madsen et al. (personal communication, 1993) provide more on errors induced by DEM misregistration.) Finally, since the interferogram phases are all measured modulo 2π, the absolute, or even relative, phase relationship between arbitrary points

Paper number 94JB01179.
0148-0227/94/94JB-01179$05.00

in the scene is difficult to determine. Thus it is virtually impossible to fit continuous two-dimensional models of the displacement field to the observations.

These limitations aside, it is important to realize that the phase displacements due to motion in an interferometric DEM can be hundreds of times more sensitive than simply differencing the actual height measurements before and after an event (see below). More complete use of phase information allows the interferometric approach to map centimeter scale distortions over a region many tens of kilometers in size at a resolution of a few meters.

In this paper, we approach the Landers analysis differently from Massonet et al. by utilizing only data acquired by the ERS 1 satellite. Our approach overcomes the aforementioned limitations and hence is more readily quantifiable given the radar system parameters, and the quality of the result can be measured "up front." Specifically, imprecision introduced by the USGS DEM in the CNES study is not present, coregistration occurs automatically in forming the interferograms, and the entire usable phase field is "unwrapped," meaning that the displacement at each point is known digitally in an absolute sense. Unwrapping renders the displacement field more amenable to computer modeling and analysis and permits the precision of the technique to be increased from the 2.8-cm radar line of sight reported by Massonet et al. to about 0.2 cm obtained here. Further, we verify the accuracy of the measurements by comparing to a displacement field derived from conventional surveying techniques. These survey data were derived from a combination of electronic distance measurement (EDM) lines and Global Positioning System (GPS) satellite receivers. The methods and results presented here can serve as a baseline for the design of a seismic monitoring program.

The structure of the paper is as follows. We begin by summarizing the theory of radar interferometry and differential interferometry, error sources, and expectations of performance for seismic studies. Next, we present the set of differential radar interferometric observations of the Landers earthquake and discuss their accuracy. Finally, we compare our results with those of the earlier study and with the in situ measurements made by GPS techniques.

Summary of Theory

In this section we derive the equations needed for calculating ground displacement fields from interferometric synthetic aperture radar measurements. Here we assume that the reader has a general knowledge of radar remote sensing systems. The interested reader may consult a general text on radar remote sensing such as that by *Elachi* [1988] or by *Curlander and McDonough* [1991] for questions on radar system operation and processing. As for information on the technique of radar interferometry, much of the work is still too new for general textbooks, and thus the technical literature is the only source available. We cite the major relevant papers in this text, and the reader may consult these when appropriate.

A side-looking spaceborne synthetic aperture radar system may map a continuous swath many tens of kilometers in width as the satellite progresses along its orbit track, yielding measurements of the amplitude and phase of radar echoes associated with independent patches on the ground perhaps 10 m in size: this size is the resolution of the radar. We first examine the case where no ground movement between radar observations occurs. Consider two radar systems observing the same ground swath from two positions A1 and A2, respectively, as illustrated in Figure 1. The measured phase at each point in each of the two radar images may be taken as equal to the sum of a propagation part proportional to the round-trip distance traveled and a scattering part due to the interaction of the wave with the ground. If each resolution element on the ground behaves the same for each observation (see more on this important condition below), then calculating the difference in the phases removes dependence on the scattering mechanism and gives a quantity dependent only on geometry. If the two path lengths are taken to be ρ and $\rho + \delta\rho$, the measured phase difference ϕ will be

$$\phi = \frac{4\pi}{\lambda}\,\delta\rho \tag{1}$$

or 2π times the round-trip distance difference in wavelengths. The law of cosines permits solution for $\delta\rho$ in terms of the imaging geometry as follows. Then

$$(\rho + \delta\rho)^2 = \rho^2 + B^2 - 2\rho B \sin(\theta - \alpha) \tag{2}$$

where the baseline length is B, the range to a point on the ground is ρ, the look angle is θ, and the angle of the baseline with respect to horizontal at the sensor is α. Neglecting the term of order $(\delta\rho)^2$ yields

$$\delta\rho \approx B \sin(\theta - \alpha) + \frac{B^2}{2\rho}. \tag{3}$$

For simplicity in describing the approach we used, we can make a second approximation, although it is not necessary for the analyses presented below. In the case of spaceborne geometries we can ignore the second term on the right-hand side of (3) and obtain

$$\delta\rho \approx B \sin(\theta - \alpha) \tag{4}$$

or

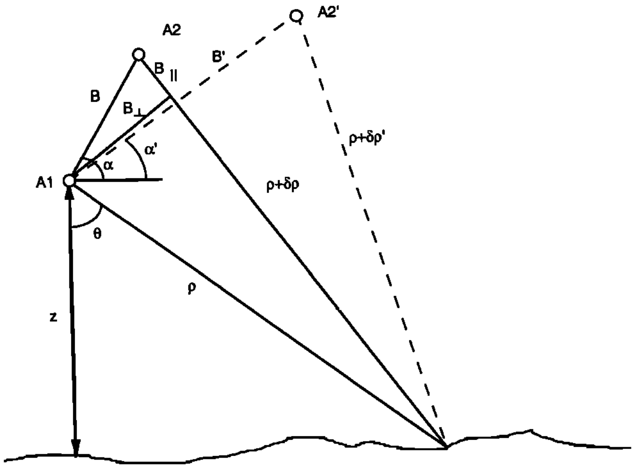

Figure 1. Radar imaging geometry. The solid lines show that radar signal paths for the first interferogram pair formed by antennas at A1 and A2. Dashed lines show signal path for second interferogram acquired over the same site but with antennas located at A1 and A2′.

$$\delta\rho \approx B_{\parallel}. \quad (5)$$

$B_{\parallel} = B \sin(\theta - \alpha)$ is simply the component of the baseline parallel to the look direction. This is the parallel-ray approximation used by *Zebker and Goldstein* [1986] in their initial paper on topographic mapping.

Equations (1) and (4) show that the measured phase of an interferometer is the component of the interferometer baseline parallel to the look direction to a given point on the surface measured in wavelengths, multiplied by two for round-trip travel. We note that the height sensitivity of the instrument enters through the dependence of the exact look angle θ on the altitude $z = h - \rho\cos\theta$, where h is the height of the sensor above the reference surface.

If a second (denoted by a prime) interferogram is acquired over the same area, sharing one orbit with the previous pair so that ρ and θ are unchanged (dashed lines in Figure 1), we can compare the interferogram phases with each other. This second interferogram is acquired with a different baseline B' and baseline orientation α', thus a different $B'_{\parallel}$. Combining (1) and (4) above, we obtain

$$\phi' = \frac{4\pi}{\lambda} B'_{\parallel}. \quad (6)$$

Examination of the ratio of the two phases yields

$$\phi/\phi' = B_{\parallel}/B'_{\parallel}. \quad (7)$$

In other words, the ratio of the phases is equal to the ratio of the parallel components of the baseline, independent of the topography.

Now consider the situation of two interferograms acquired over the same region as before but in this case an earthquake has displaced each resolution element between observations for the primed interferogram. The displacements are assumed small with respect to a resolution cell so that the radar echoes remain correlated. Here in addition to the phase dependence on topography there is a phase change due to the radar line of sight component of the displacement $\Delta\rho$. In this interferogram the phase ϕ' will be given by

$$\phi' = \frac{4\pi}{\lambda}(B'_{\parallel} + \Delta\rho). \quad (8)$$

The displacement term $\Delta\rho$ adds to the topographic phase term, creating confusion in the interpretation of the result. However, if the data from the initial unprimed interferogram are scaled by the ratio of the parallel components of the baseline and subtracted from the primed interferogram, we can obtain a solution dependent only on the displacement of the surface, as follows

$$\phi' - \frac{B'_{\parallel}}{B_{\parallel}}\phi = \frac{4\pi}{\lambda}\Delta\rho. \quad (9)$$

Since the quantity on the left is determined entirely by the phases of the interferograms and the orbit geometries, the line of sight component of the displacement $\Delta\rho$, is measurable for each point in the scene.

The ratio

$$\frac{B'_{\parallel}}{B_{\parallel}} = \frac{B' \sin(\theta - \alpha')}{B \sin(\theta - \alpha)} \quad (10)$$

is a function of the angle θ, which depends both on the illumination geometry and also the topography at each point in the radar image. To evaluate (9) via (10) directly, we must solve for the topographic map of the area of interest from the interferometric data or obtain the elevation data from another source. In the interests of simplicity and accuracy, we have devised an indirect approach for which it is not necessary to implement the step of either topographic solution or registration of dissimilar data sets.

We remove from the interferogram phase a term that would exist even in the absence of topography on a spherical Earth. The phase corrected for the "curved Earth" effect, denoted ϕ_{flat}, is given by

$$\phi_{\text{flat}} = \frac{4\pi}{\lambda}[B\sin(\theta - \alpha) - B\sin(\theta_0 - \alpha)], \quad (11)$$

where θ_0 is the look angle to each point in the image assuming zero local height. The interferogram phase after this correction represents the distortion of the interference grating pattern due to topographic variation relative to a spherical surface and displacements due to motion in the scene. The interferograms shown throughout this paper have been "flattened" according to (11).

Noting that the deviation of the exact θ from θ_0 is small, we can expand the first term on the right-hand side of (11), leading to

$$\phi_{\text{flat}} = \frac{4\pi}{\lambda}\delta\theta B\cos(\theta_0 - \alpha), \quad (12)$$

where $\delta\theta = \theta - \theta_0$. Numerically, ϕ_{flat} is equal to the product of the perpendicular component of the baseline $B_{\perp}$, assuming no topography is present on the surface, and the topographic angular distortion $\delta\theta$. Thus the ratio $\phi_{\text{flat}}/\phi'_{\text{flat}}$ is now in terms of θ_0 rather than θ and depends only on the viewing geometry and the baseline. If we now restate the differential phase equation (9) above in terms of the flattened phase ϕ_{flat}, we obtain

$$\phi'_{\text{flat}} - \frac{B'_{\perp}}{B_{\perp}}\phi_{\text{flat}} = \frac{4\pi}{\lambda}\Delta\rho. \quad (13)$$

With this function, we can now solve directly for the displacement $\Delta\rho$ without requiring the exact values of θ, and hence the topographic information, at an intermediate step. We have used this procedure (equation (13)) for the reduction of the data presented in this paper.

We note that if the baseline used in the flattening operation (equation (11)) is not exactly the true baseline value, (12) will contain error terms and the subsequent displacement maps will be distorted. This condition is described in detail in the appendix; for the rest of this paper we will assume that the correct baseline values are used.

We have shown that the phase in radar interferograms depends both on the local topography and on any motion that may occur between viewing instances. We may compare the sensitivity of the phase measurement to the phenomena of topography and displacement, which may be derived by differentiating (8) with respect to height through $B_{\parallel}$ and displacement. In the first case, using $dz = \rho\sin\theta\, d\theta$, obtained from the dependence of height on angle described above, we find

$$d\phi' = \frac{4\pi}{\lambda} B \cos(\theta - \alpha)\, d\theta \tag{14}$$

and

$$\frac{d\phi'}{dz} = \frac{4\pi}{\lambda} \frac{B \cos(\theta - \alpha)}{\rho \sin \theta}. \tag{15}$$

For the displacement case we have

$$\frac{d\phi'}{d\Delta\rho} = \frac{4\pi}{\lambda}. \tag{16}$$

Since the distance ρ typically is very much greater than the baseline distance B, it is evident from (15) and (16) that a much more sensitive dependence of phase results from displacements than from topographic variation. In other words, the system is more sensitive in an absolute sense to surficial change than to the topography itself. Comparing the two results numerically, for the April–August ERS 1 case described here (see next section), 1 m of topography gives a phase signature of 4.3°, while for the same pass pair a 1-m surface displacement yields a phase signature of 12800°, or nearly 3000 times greater sensitivity. Thus, while radar interferometry can be used to measure topography to an accuracy of meters, displacements may be determined to the centimeter or millimeter level.

This ratio of sensitivities illustrates the power of the interferometric technique to detect small changes. If, for example, we chose to map seismic displacements by differencing DEMs, whether acquired interferometrically or by conventional stereo photogrammetry, changes would only be visible if they were significant in size compared to the uncertainty of the DEM measurement, which is typically meters. For the interferometric case in the previous paragraph, for example, system noise limits the useful signatures to those causing a phase shift greater than about 20°, or 4.6 m. While thus permitting topographic mapping with a vertical precision of 4.6 m (H. A. Zebker et al. (personal communication, 1993) give a discussion of ERS 1 DEMs with this precision), a worthwhile result for many applications, it is not particularly useful for the study of earthquakes. In contrast, if data are acquired with an interferometric pair that spans the seismic event, even 1 cm of line of sight displacement results in a signature of 64°, easily detectable in ERS 1 data.

There are, however, two very important limitations to the interferometric technique. First, radar echoes acquired on the three passes must correlate with each other; that is, the signals must be substantially similar over a significant period of time. Physically, this translates to a requirement that the ground scattering surface be relatively undisturbed at the radar wavelength scale between measurements. Several studies have addressed this phenomenon, both theoretically [e.g., *Li and Goldstein*, 1990], and experimentally [e.g., *Gray et al.*, 1993]. *Zebker and Villasenor* [1992] were able to model and quantify the temporal decorrelation process and found that different surfaces decorrelate at different rates. This limits the applicability of the approach to areas that do not change much with time. Some regions, such as desert areas, may exhibit very little decorrelation over long periods. In the data presented here, correlation was usably high even after 105 days, the longest time period examined. From this we conclude that the radar properties of the desert surface change little over months if weather and other environmental factors are not altering the condition of the ground significantly.

The second limitation, more important for this study, is that the phases must be "unwrapped" before data from one interferogram may be used to correct the second interferogram (equation (9)) to estimate the displacement phases. The measurements of each phase are known only modulo 2π, and various techniques exist [*Goldstein et al.*, 1988; *Ghiglia and Romero*, 1993; A. Hiramatsu, personal communication, 1992] to determine the absolute phase relationship between all arbitrary points in a data set (that is, unwrapping). While not fully characterized in any of the existing literature, it is apparent that the ability to unwrap arbitrary phase fields depends on two factors: the noise level in the system and the interferometric fringe spacing. For the July–August pair described here in particular, the interferometric baseline is quite large, being 40% of the critical baseline at which no correlation between signals is possible. (For a more complete discussion on baseline decorrelation, see *Zebker and Villasenor* [1992]). Since the fringe rate depends on local surface slope, typically it is more difficult to estimate phases reliably in rough terrain than in flat terrain if the fringe rate is high to begin with. The result of this is that we were unable to obtain reliable phase estimates in the rougher regions, as will be seen in the data presented below.

ERS 1 Interferograms of the Landers Earthquake

The ERS 1 radar system, operating at a wavelength of 5.67 cm, images Earth from an altitude of about 790 km and produces radar backscatter maps of 100-km-wide swaths at a resolution of about 25 m across track and 6 m along track. We obtained raw ERS 1 radar signal samples acquired over the Landers region on April 24, July 3, and August 7, 1992. We combined these to form two interferograms, one from the April–August pair and one from the July–August pair. The April–August pair spans the June 28 earthquake and was chosen over the April–July pair which exhibited an exceptionally large baseline. No data were acquired on May 29 when the satellite again passed over the site. Orbit reconstructions provided by the European Space Agency (ESA) enabled us to determine the geometrical parameters for the pairs chosen as given in Table 1. The parallel baseline components given in Table 1 are for a look angle of 21°. Since the radar swath is quite wide, the actual look angle varies from about 17° to 23° and the parallel components vary somewhat.

The Landers area is shown in Figures 2a and 2b, where the faults shown, illustrated by heavy lines, are those affected by the Landers earthquake and imaged by the ERS 1 radar.

Table 1. ERS 1 Landers Interferometer Baseline Parameters

Pair	Baseline B, m	Orientation α, deg	Parallel Component $B_\parallel$, m	Perpendicular Component $B_\perp$, m
April–August	146.1	152	110.3	95.8
July–August	503.1	175	220.5	452.2

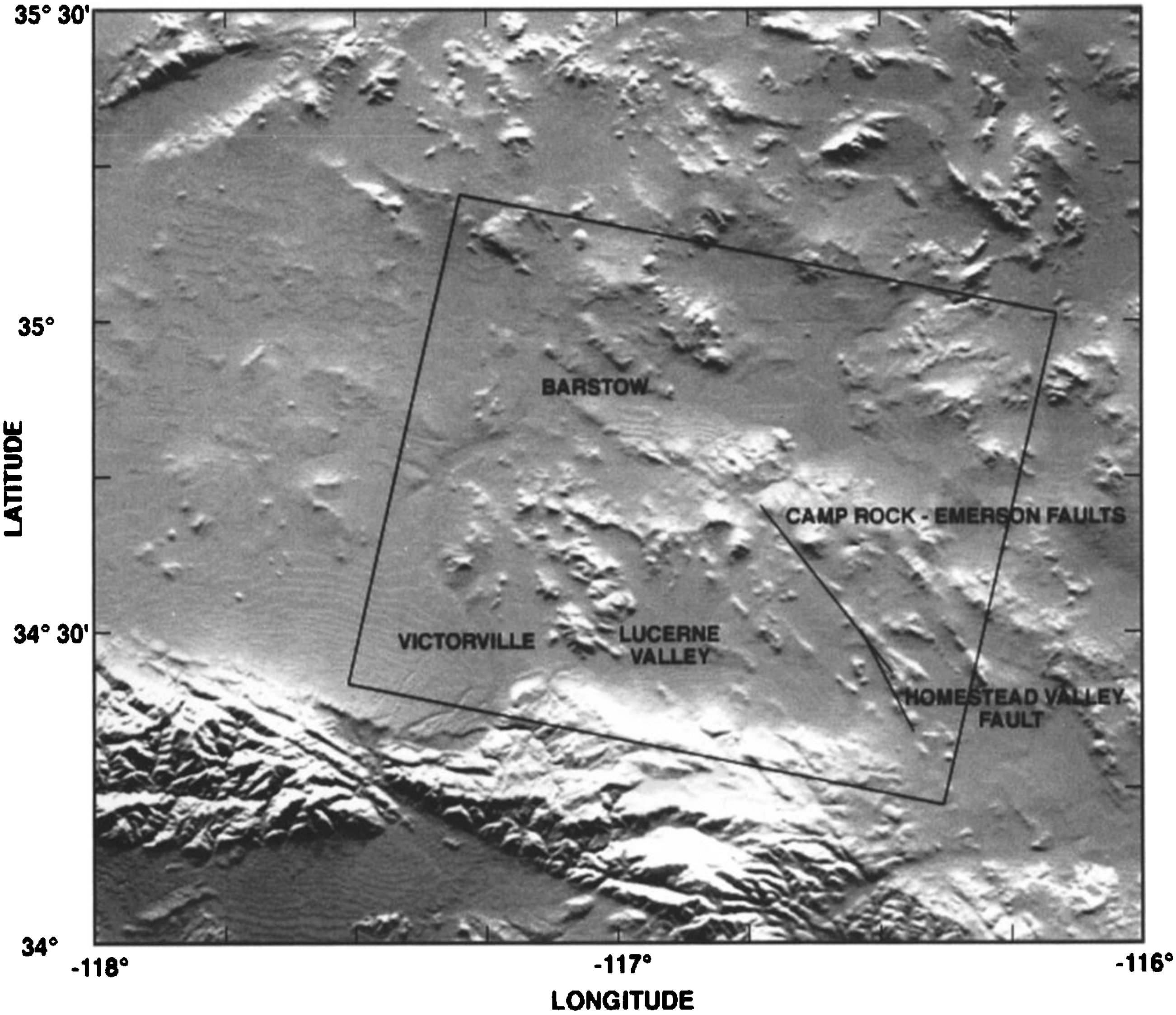

Figure 2a. Shaded relief map derived from USGS DEM with geographic features shown for reference. The inset rectangle is the region of the ERS 1 radar swath analyzed here. Also noted are the approximate position of the Camp Rock–Emerson and Homestead Valley faults. The cities of Barstow, Victorville, and also Lucerne Valley area are shown for reference.

Figure 2a is a shaded relief representation of the region: limits of the ERS 1 data we analyzed are indicated by the rectangle. Figure 2b is the radar backscatter image with two further areas denoted in addition to the faults. It represents an area roughly 113 km by 90 km. These data, as well as the radar images below, are in a radar slant range and along-track direction coordinate system. Radar slant range, denoted by ρ in Figure 1, here means that the across-track distances given are in terms of line of sight distance of each point to the radar rather than that distance projected on the ground. That is, the data have not been geocoded, or placed in map coordinates. We have preserved the "natural" spacing of the data points in order to maintain the highest possible signal fidelity throughout the processing procedure. However, we do apply a geocoding transformation before comparison with the field survey results described in the following section.

We processed the radar signal samples at the Jet Propulsion Laboratory (JPL) using a software processor constructed specifically by us for ERS 1 interferometric applications. The data were processed using a range-Doppler algorithm, but the range-compressed signals were filtered for the July–August pair using the method suggested by F. Gatelli et al. (personal communication, 1993) to reduce baseline decorrelation. We found that this approach yielded about 5–10% greater correlation in some regions at the expense of a slight reduction in range resolution. More information on radar processing approaches can be found in the general radar textbooks described previously.

The interferograms obtained in this process are shown in Plate 1, with the corresponding correlation coefficient maps shown in Plate 2. The top image in each case represents the April–August interferogram, while the bottom image shows data from the July–August pair. The June 28 earthquake effects are found in the April–August pair. In these plots the fringe signature of a curved Earth surface, as described in

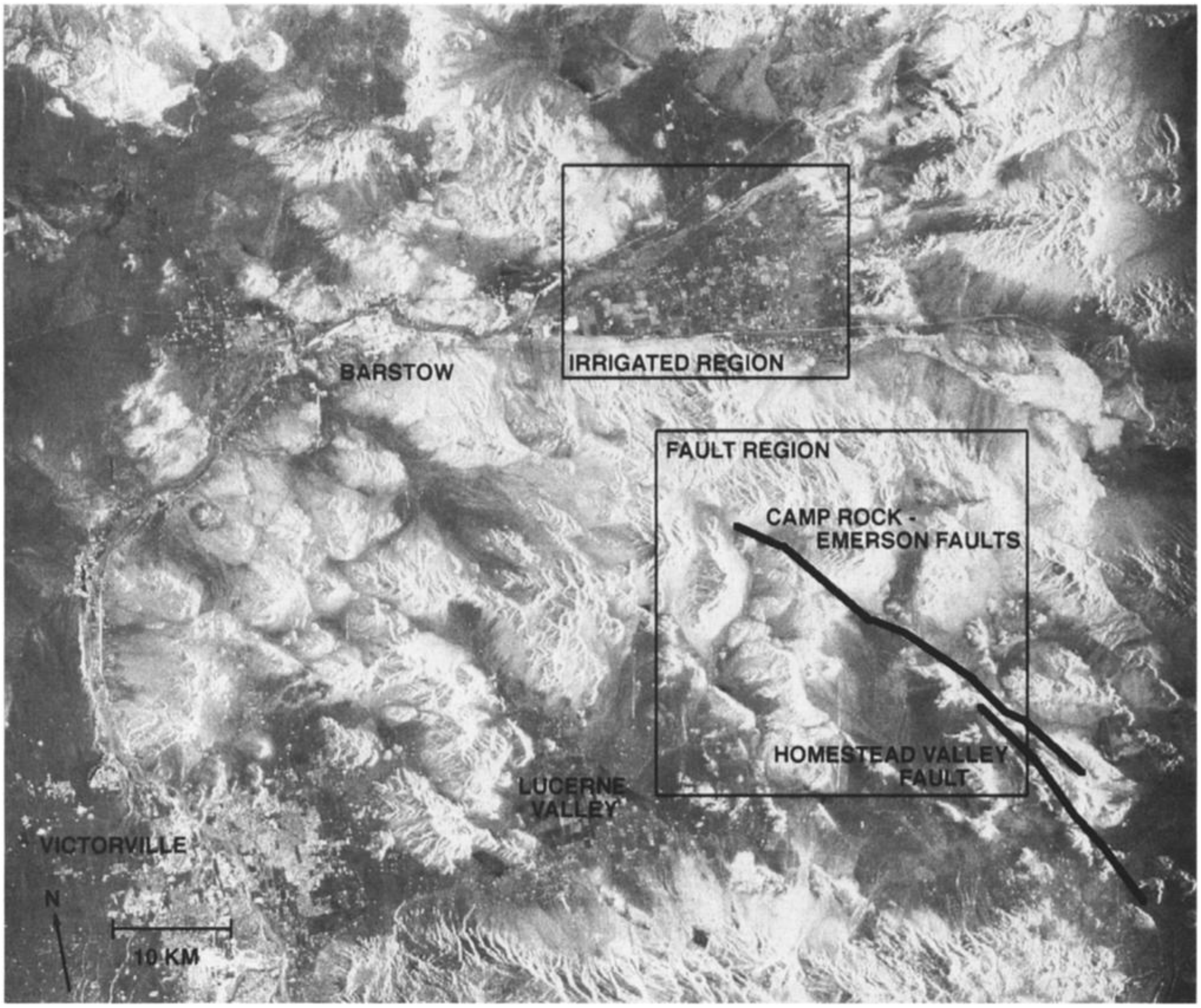

Figure 2b. Radar image of the Landers area, where the fault locations are illustrated by the heavy lines. The radar image covers an area on the ground approximately 113 km by 90 km. Insets of an irrigated region as well as a fault zone are shown for later reference. These data, as well as the radar images in the remaining figures, are in a radar slant range and along track direction coordinate system.

the section on theory above, has been removed from the interferograms for clearer display. Note that the very high fringe rates, and corresponding loss of correlation, in the mountainous regions for the July–August pair, lead to our inability to unwrap the phase in these regions. Also note in the April–August pair a similar loss of correlation in the fault zone, presumably due to (1) very high fringe rates of greater than one cycle per resolution element, (2) large ground shifts resulting in lack of precision alignment of the pixels from pass to pass, and (3) rearrangement of the surface at the wavelength scale from the earthquake itself.

These interferograms were filtered using a spatially variable bandpass filter that selected the optimal fringe rate passband in each 32 by 32 pixel subregion in the interferogram. In this process we also identified areas of low fringe visibility to serve as a mask in the final product, eliminating regions where we felt we could not trust the phase estimates. The data were then unwrapped using the method of A. Hiramatsu (personal communication, 1992), which is an extension of the method first presented by *Goldstein et al.* [1988].

Finally, the differential interferogram was calculated by scaling the July–August measurement by the ratio of the parallel baseline components for each look angle and subtracting that value from the corresponding value in the April–August pair. The result is a map of the displacements of the ground in the radar line of sight direction (equation (9)), shown in Plate 3, where the shift is coded by color and the brightness at each point is the radar image brightness. In addition, contour lines representing line of sight displacements spaced every 5 cm are shown.

It must be noted that the earthquake is not the only process affecting the phase measurements in this region of the Mojave. Plate 4 is an enlargement of the April–August interferogram plus the correlation coefficients for the region east of Barstow indicated in Figure 2 where center pivot irrigation has been employed. The irrigated circles, and some other agricultural fields, show a clear loss of correla-

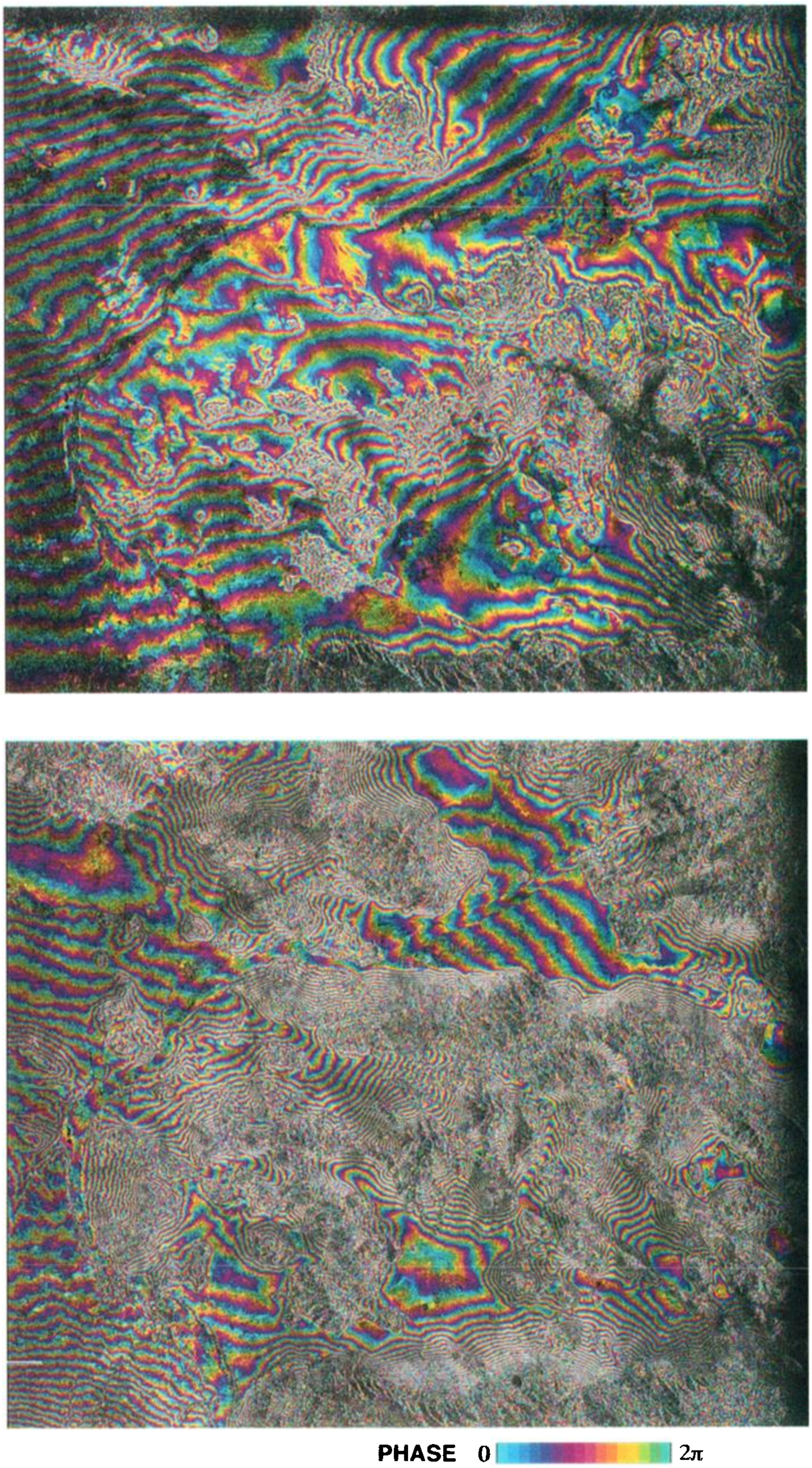

Plate 1. Interferograms of the Landers area. (top) April–August interferogram; (bottom) July–August pair. The June 28 earthquake effects are found in the April–August pair. The fringe signature of a curved Earth surface has been removed from the interferograms for clearer display. Note the very high fringe rates in the mountainous regions for the July–August pair, leading to our inability to unwrap the phase in these regions.

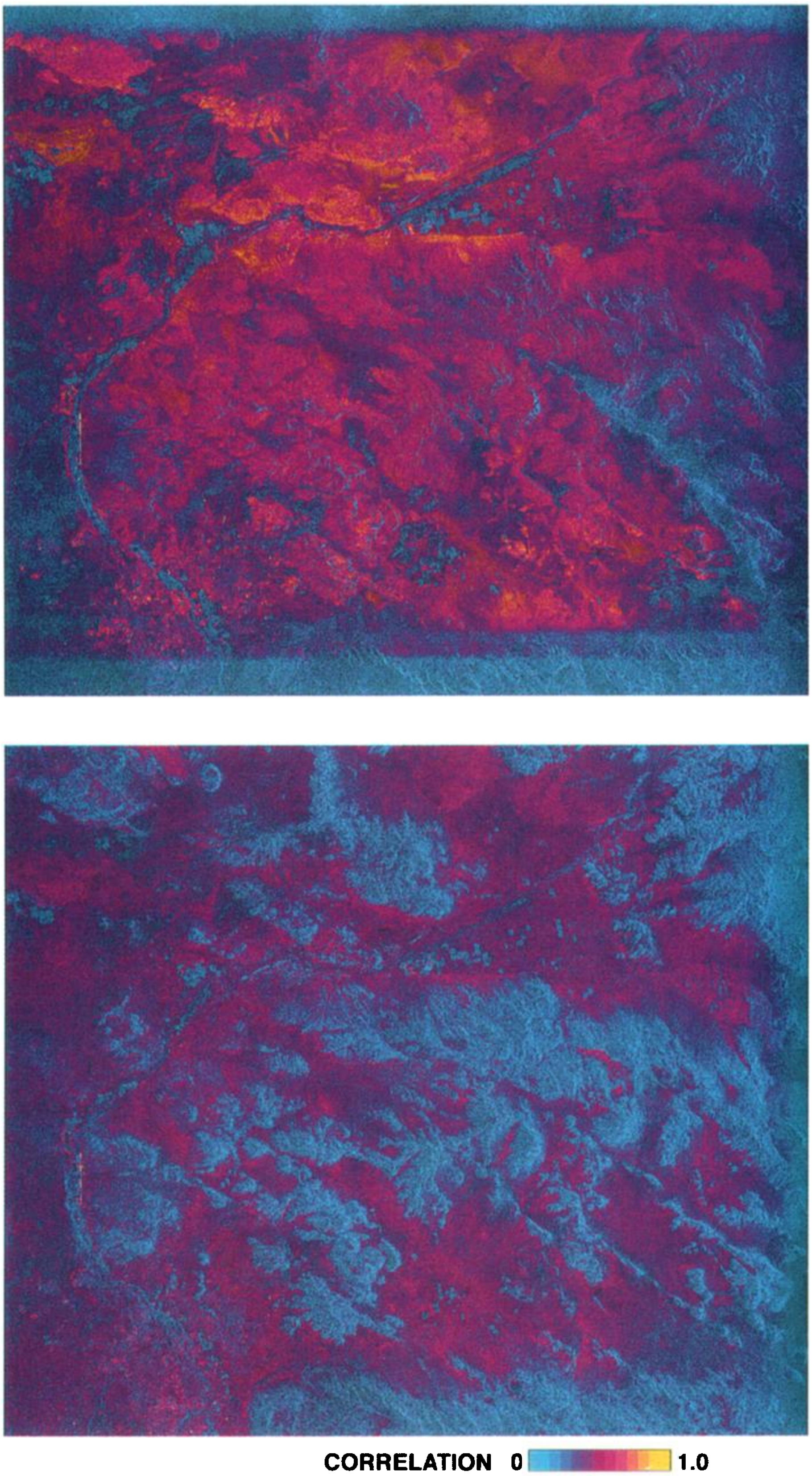

Plate 2. Corresponding correlation coefficient maps to interferograms of Plate 1. (top) April–August; (bottom) July–August. Note in the April–August pair a loss of correlation in the fault zone, presumably due to (1) very high fringe rates of greater than one cycle per resolution element, (2) large ground shifts resulting in lack of precision alignment of the pixels from pass to pass, and (3) stirring up of the surface at the wavelength scale from the earthquake itself.

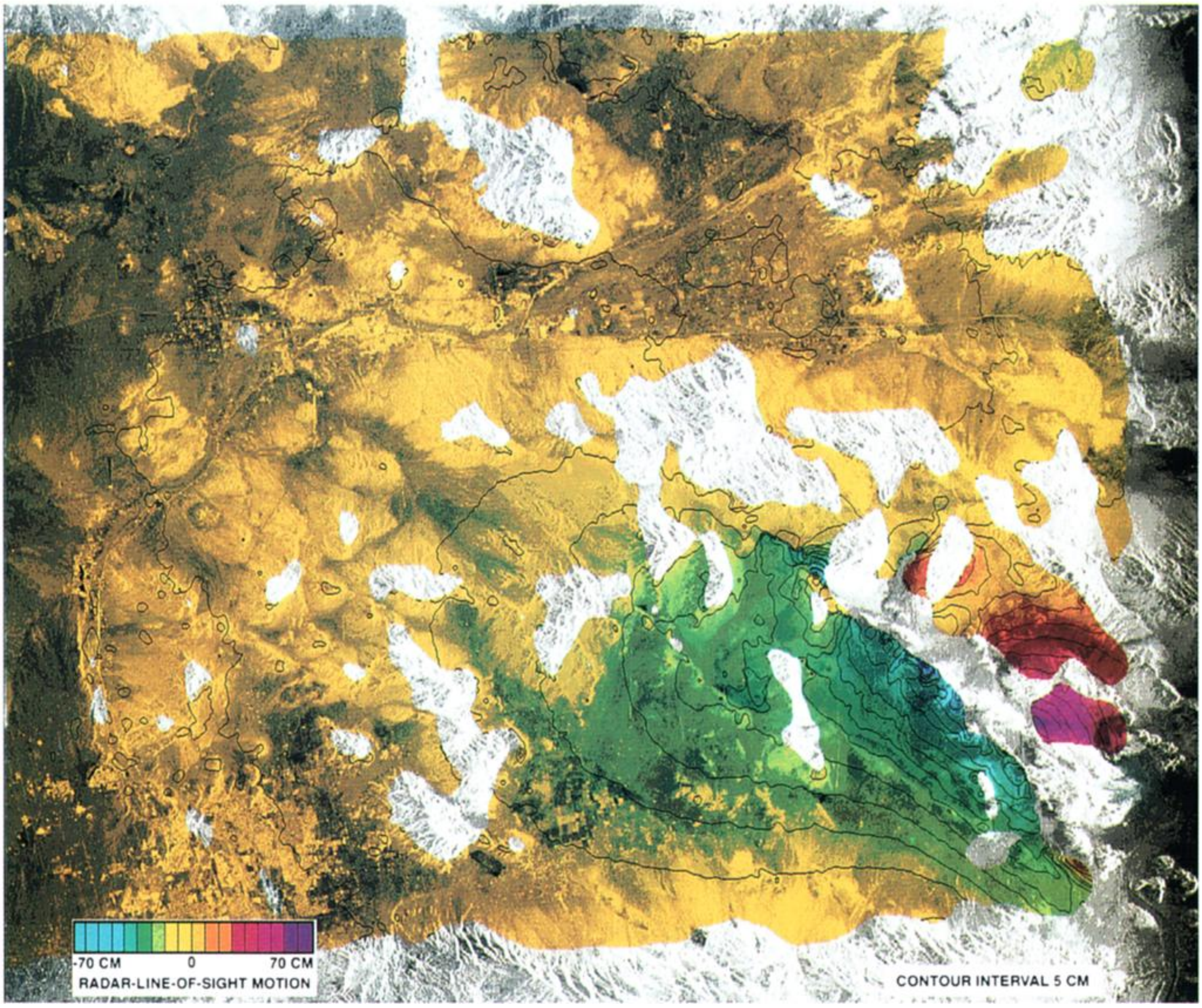

Plate 3. Differential interferogram of the Landers earthquake region. Radar line of sight displacements are coded in color, ranging from −70 to 70 cm, while the radar reflectivity of the surface is shown as brightness. Contours indicating each 5 cm of displacement are drawn in black.

tion presumably due to crop growth and phase shifts which are due to motion, not topography (it is a flat area). *Gabriel et al.* [1989] found similar surface displacements of several centimeters in fields that had been irrigated over a 9-day period. The motions observed in this image as well could be caused by changes in the surface elevations from pumping underground water or other hydrologic effects.

Since one of the strengths of this technique is its intrinsic high spatial resolution, we also show in Plate 5 an enlargement in the April–August interferogram of the region around the fault zone shown in Figure 2b. The phases in an interferogram are not unwrapped and so should not exhibit discontinuities except in regions of severe layover (where the surface slopes are greater than or equal to the radar incidence angle, resulting in severe image distortion) unless spatially discontinuous motions (breaks) occurred during the period spanned by the interferogram pair. Nevertheless, Plate 5 shows clear discontinuities in relatively flat areas. For example, the region denoted A in Plate 5 shows a clear break in the phase measurements. A similar break does not occur in the July–August pair, and therefore the April–August discontinuity must be due to a displacement of the surface where one piece moved more than the other. This cracking effect is more pronounced in the region denoted B, shown enlarged again in Plate 6, where the cracking is so extensive that it seems the ground has been broken into many tiles each several hundred meters across. These data are shown in unwrapped form. The phase unwrapping algorithm we use must identify phase discontinuities before calculating the absolute phase values; the locations of cuts determined automatically by our algorithm are shown in black. Presumably, these phase discontinuities are representations of centimeter-scale displacement discontinuities on the surface resulting from the earthquake. It would be an interesting field exercise to compare the computer generated cuts with any visible surface scars.

We also present in Plate 7 a perspective view of the entire area shown in Figure 2b where the vertical scale is proportional to the displacement in the radar line of sight of the surface. As usual, the brightness at each point is related to

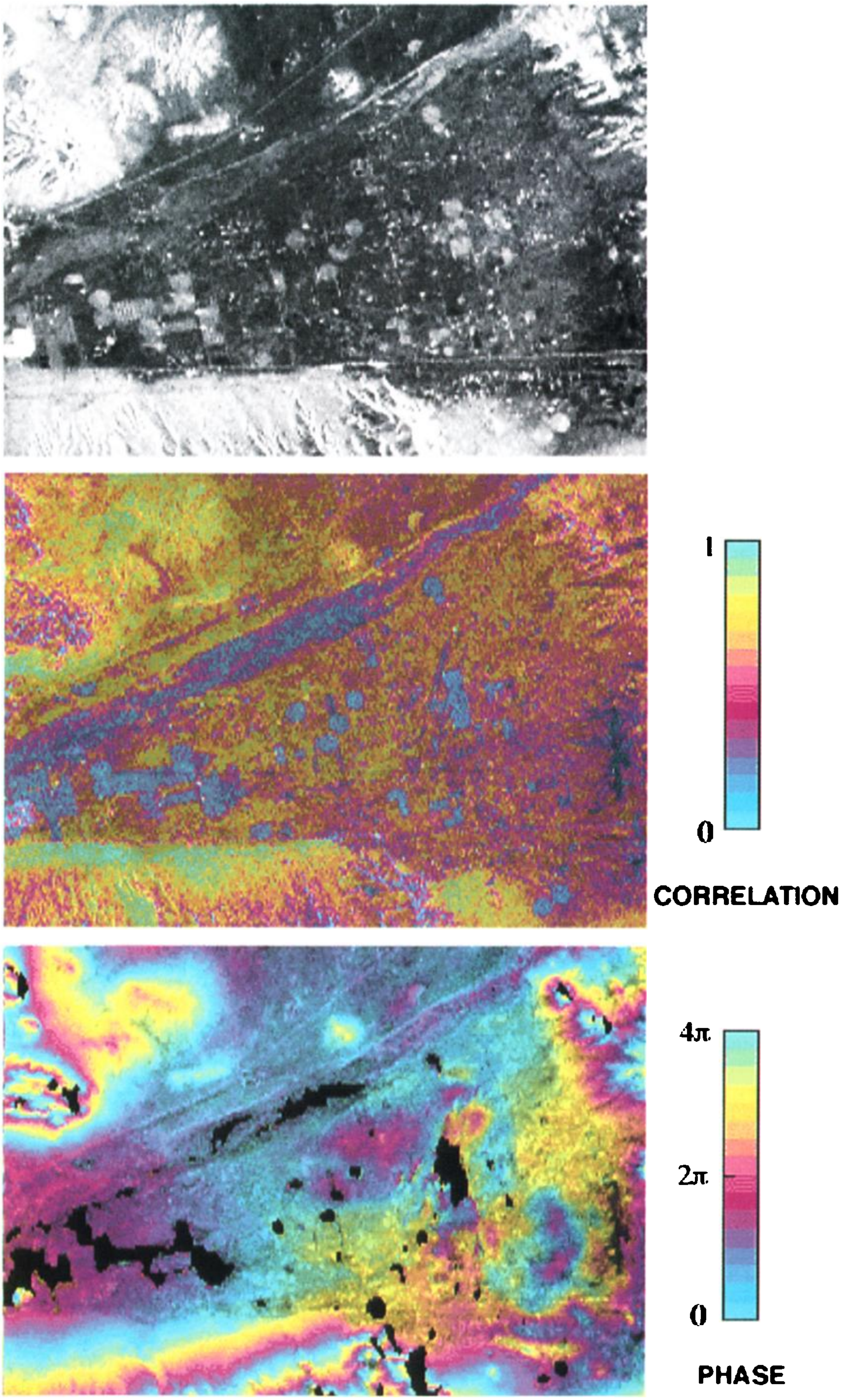
1
0
CORRELATION
4π
2π
0
PHASE

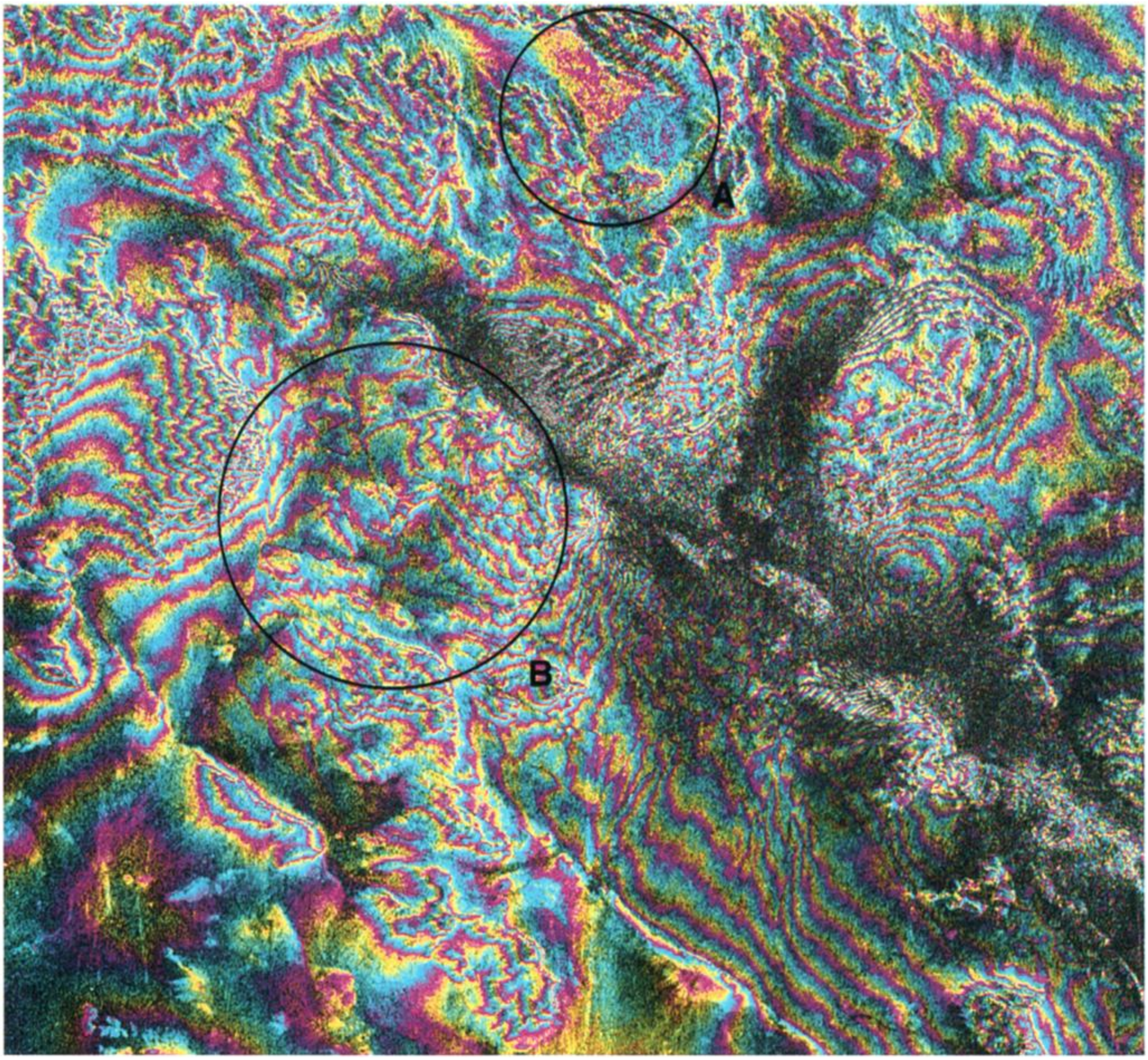

Plate 5. Enlargement in the April–August interferogram of a region around the fault zone. The region denoted A shows a clear break in the phase measurements, which must be due to a displacement of the surface where one piece was displaced more than the other. More extensive cracking is found in region B (see Plate 6).

Plate 4. (opposite) Enlargement of the April–August interferogram plus the correlation coefficients for a region east of Barstow where center pivot irrigation has been employed. (top) Radar reflectivity, (middle) correlation coefficient, and (bottom) unwrapped interferogram. Black spots in the lower image are where correlation was insufficient for reliable phase estimates. The irrigated circles show a clear loss of correlation, presumably due to crop growth, and phase shifts which are due to motion, not topography. Examination of the mountains at the top left of the image shows that a topographic change of over 150 m is necessary to cause a one cycle change in phase, and the area in question shows less than 30 m topographic variation. These phase changes could be caused by changes in the surface elevations from pumping underground water or other hydrologic effects.

radar reflectivity, while the color is the displacement mapped into a repeating color table to accentuate the visibility of the changes to produce a contour-like map. From this view one can see that the displacement increases as the fault is approached at which point there is an abrupt break in the surface; from this point hence the surface displacement is of opposite sign.

We assess the internal consistency and accuracy of the measurements presented here by three separate calculations. First, we calculate the expected errors due to statistical variation of the phase estimates. Assuming a radar signal to noise ratio of 6 dB for the flat desert surfaces, our 20 equivalent look processing (20 resolution elements are spatially averaged to reduce statistical noise) yields a stan-

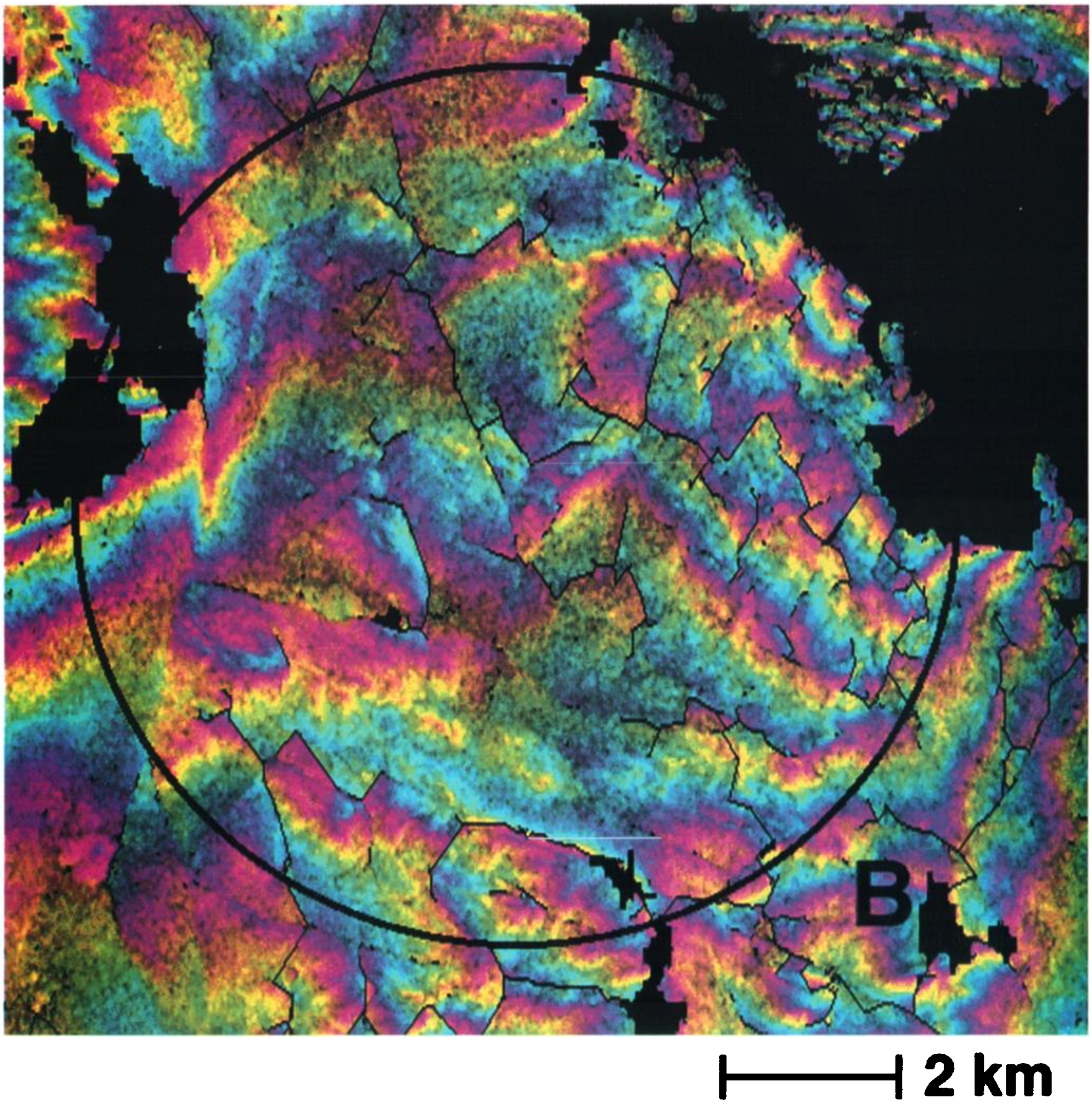

Plate 6. Region B from Plate 5, showing phase data in unwrapped form. The phase unwrapping algorithm we use identifies phase discontinuities before calculating the absolute phase values, and the locations of cuts determined automatically by our algorithm are shown in black. These phase jumps likely correspond to ground discontinuities at the cm level that appeared between April and July 1992, probably coincident in time with the earthquake. Cracking is so extensive that it seems the ground has been broken into many tiles each several hundred meters across.

dard deviation of 9.5° in the phase for the geometry of the April–August interferogram and 14.5° for the July–August interferogram; these values follow from using a target radar cross section of −17 dB and accounting for losses accruing from illuminating the ground off the boresight of the antenna. Combining these yields an expected phase error of 10° rms for the differential interferogram, equivalent to a horizontal displacement noise due to finite signal to noise ratio and baseline decorrelation of 0.2 cm. We would expect this value to be an underestimate as it does not take into account any temporal decorrelation due to surface disturbances or additional processing artifacts such as misregistration or other sampling and interpolation errors.

Second, we empirically determined statistical variations by measuring the observed phase standard deviations and converting the result to horizontal displacement errors. Choosing boxes corresponding to about 400 m by 400 m of the surface in areas of little seismic variation yielded an

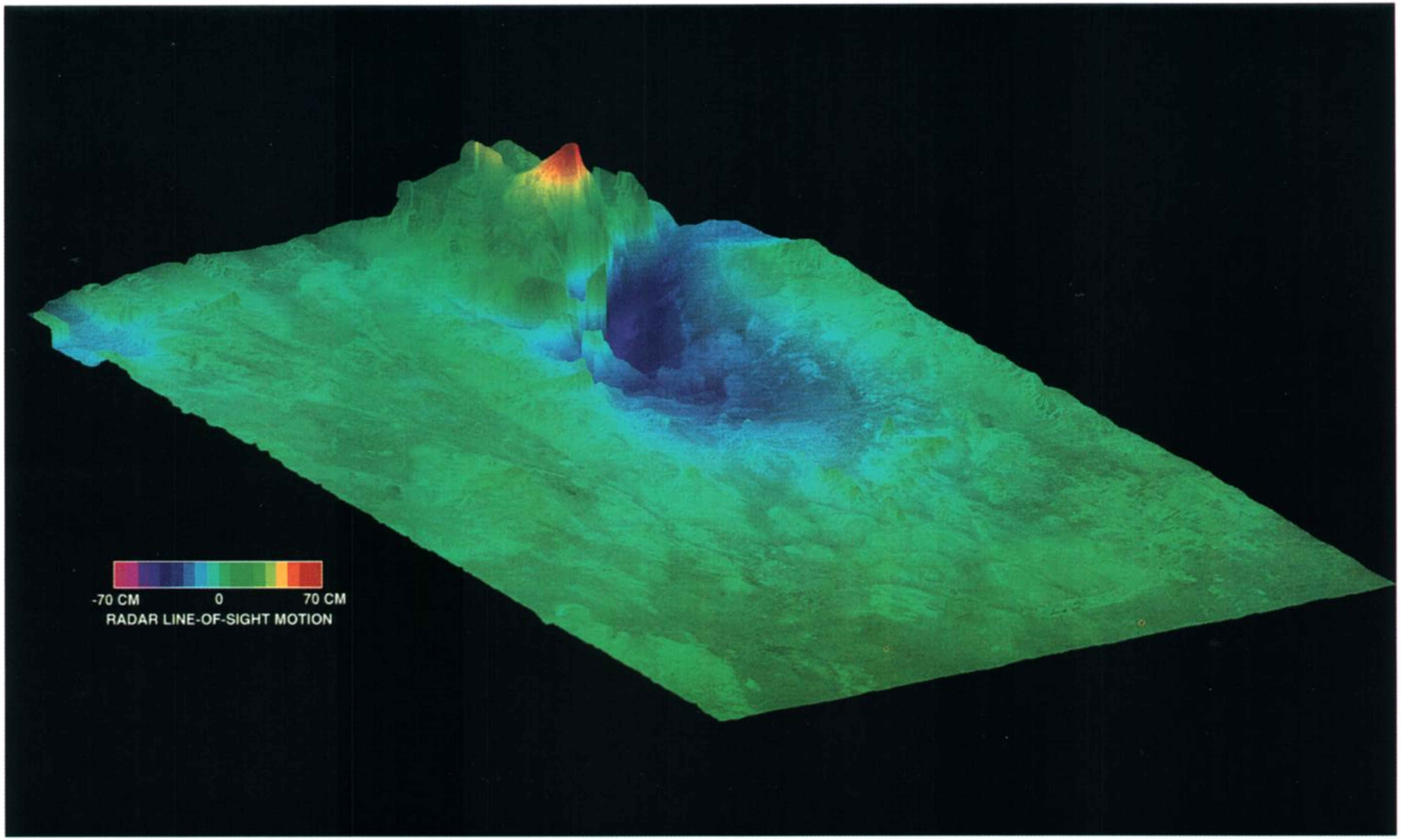

Plate 7. Perspective view of the region where the vertical scale is proportional to the surface displacement in the radar line of sight. The brightness at each point is related to radar reflectivity, while the color is the displacement. The color repeat interval is 140 cm. The displacement increases as the fault is approached at which point there is an abrupt break in the surface.

Table 2. Comparison of Radar and GPS Motion Estimates

Site	Latitude, deg	Longitude, deg	Horizontal Displacement for Observed Radar Motion, cm	GPS Vector in Radar Direction, cm	Difference, cm
6052	34.52	−116.84	47.8	33.2	14.6
6056	34.37	−116.65	18.1	21.9	−3.8
7000	34.68	−116.72	36.8	91.1	−54.3
7001	34.56	−116.47	−37.1	−70.2	33.1
HECT	34.79	−116.42	9.7	−5.2	14.9
LAZY	34.34	−116.51	62.9	49.4	13.5
LUCS	34.44	−116.88	26.4	20.7	5.7
POIN	34.45	−117.07	13.4	9.5	3.9
SOAP	34.90	−116.98	12.3	1.7	10.6
STIM	34.54	−117.24	7.8	7.4	0.4
FLASH	34.82	−117.02	14.1	12.1	2.0
HARVARD	34.94	−116.67	7.5	−0.4	7.9
BOULDER	34.51	−116.56	176.1	210.8	−34.7
FRY	34.50	−116.72	66.0	74.6	−8.6
MEANS	34.41	−116.55	82.2	69.8	12.4
OLD WOMN	34.39	−116.75	25.0	17.1	7.9
ORD	34.68	−116.81	44.4	48.3	−3.9
ROCK	34.54	−116.77	63.9	69.1	−5.2

average horizontal displacement of 0.4 cm rms for the high-frequency component of variations.

Finally, we attempted to address larger-scale variations by measuring the displacement at 10 widely separated locations far from the fault, and we determined their standard deviation. In this case the boxes were separated by 10 km or so, so that sensitivity to larger-scale variations would dominate. This calculation gave a horizontal displacement error component of 0.6 cm rms for these medium frequency variations, where medium frequency here refers to irregularities occurring with a spatial frequency of several cycles across the radar image.

Comparison With Field Measurements

In this section we discuss the accuracy of our measurements and compare the results to those obtained in the field using Global Positioning Satellite (GPS) and electronic distance measurement (EDM) survey data. As a basis of comparison we will use the coseismic displacement field solution as derived by J. Freymueller et al. (personal communication, 1993), data which were compiled by K. W. Hudnut et al. (personal communication, 1993). Hudnut et al. also analyzed these data and obtained a slightly different, but consistent solution. These calculated displacements were derived from a combination of GPS data from several sources and EDM line lengths obtained by the USGS (please see the above references for a more detailed description of the data sources and techniques).

The area of overlap between the field survey and our image contains 18 points at which both field data and radar estimates of the motion are available. Three additional site measurements of field data exist in the overlap region, but we were not able to obtain reliable radar phase estimates for them (they occur in the gray regions of Plate 3). As can be seen from Plate 3, however, the radar data are generally valid over a wide area and should future surveys or analyses produce additional field points, they may be easily compared with the present analysis.

As stated previously, the radar technique is sensitive to the line of sight component of motion. We therefore calculated the component of the GPS motion vectors in the direction of the projection on the ground of the radar sensor boresight, the vector from the sensor to a point on the Earth's surface. As for the radar measurements, since the line of sight direction is not in the plane defined by the local Earth surface, we derived the equivalent horizontal surface motion to yield the observed slant range displacement using

$$\Delta y = \frac{\Delta \rho}{\sin \theta_{\mathrm{inc}}} \tag{17}$$

which relates the horizontal displacement Δy to slant range displacement $\Delta \rho$ and the incidence angle θ_{inc}. This angle is equal to the look angle (denoted θ in Figure 1) for a flat Earth approximation, and is approximately equal for a curved Earth model. We use a curved Earth model for its improved accuracy. The results of both of these calculations are shown in Table 2 and Figures 3 and 4.

Because the orbit of the ERS 1 satellite is known only approximately, as discussed above there are residual tilts in the derived radar displacement field. Therefore we have removed this distortion by solving, in a least squares sense, for the planar tilt that minimizes disagreement between the radar and GPS/EDM measurements. This nicely illustrates one aspect of the complementary nature of the two techniques for analyzing ground motions: the radar measures a widespread displacement field while the GPS/EDM data provide accurate point measurements which are used to refine the radar estimates.

The mean value of the differences in Table 2 is 0.9 cm, and the rms difference is 18.9 cm. The formal correlation of the data is 0.96, which we illustrate in Figure 3, a scatter plot comparing the radar and GPS/EDM measurements. Note that the best fit through the data evidences a slight bias.

Figure 4 shows the same data of Table 2 presented graphically. For each survey site, denoted by a triangle, we illustrate vectors corresponding to motion as determined by

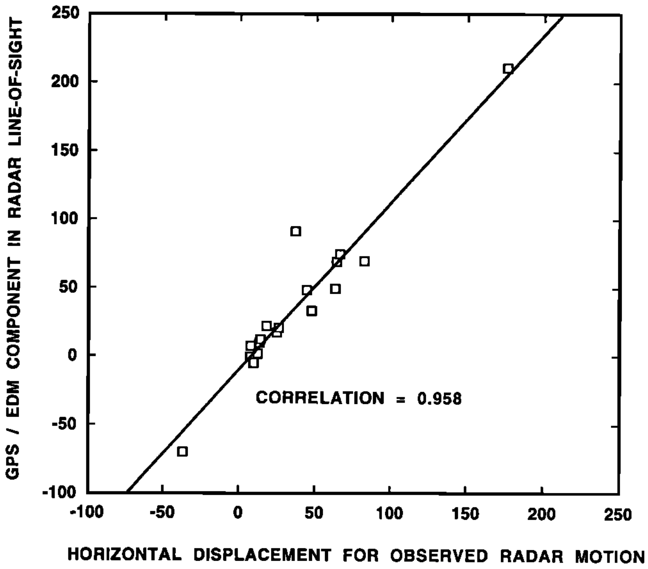

Figure 3. Scatter plot of displacement measurements with GPS/EDM data on vertical axis and radar measurements on horizontal axis. The correlation of the data sets is 0.96, however a slight bias is observed as the slope of the line is not 1.

survey techniques (diamond-headed arrows) and as determined by the radar (cross-headed arrows). Note that the radar vectors are all parallel to the edge of the radar image, as only the component of motion in the line of sight is measured.

From each of these presentations it is apparent that at most sites, with significant exception of sites 7000 and 7001, the measurements are in rough agreement. The absolute disagreement is also large at BOULDER, but the motion here is quite large, and on a relative scale the agreement is comparable to the values for the remaining sites. It is interesting to note that in the deviant cases a large motion is observed by the GPS technique, while a smaller displacement is visible by the radar technique. In each case where a small motion is detected by the field survey, a small motion is measured by the radar interferometer. Figure 4 also suggests that there is a degree of spatial correlation in the regions of agreement, that is, the amount of agreement is spatially dependent.

There are several possible causes for the disagreements in the measurements. First, the radar technique is highly sensitive to vertical motions which are not expressed in the GPS displacement field. While this is likely to affect the differences on the centimeter scale, it is probably not a significant

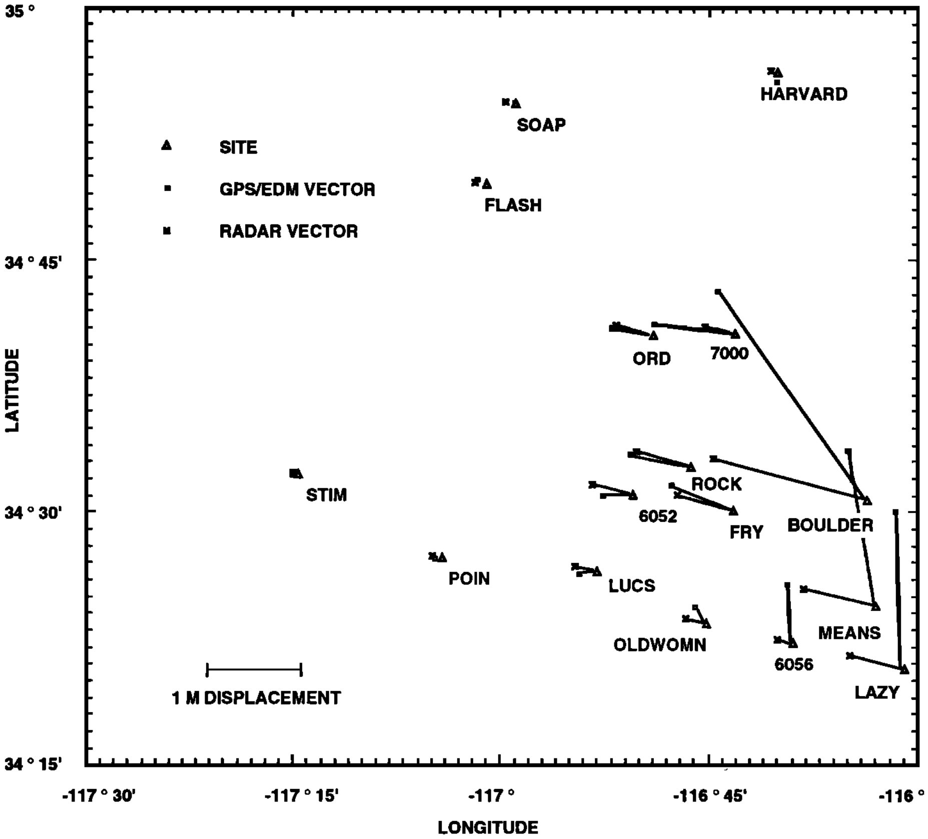

Figure 4. Displacement vectors as measured by GPS/EDM data and by radar interferometry. Each GPS or EDM site is denoted by a triangle, and a vector ending with a square (GPS/EDM measurement) and a vector ending with a cross (radar measurement) are shown in the direction of motion. Note that for the radar case only the component in the radar line of sight direction is determined and thus all measurements are parallel. Vectors are correlated at 0.96 level and show that radar and field surveys are measuring similar phenomena.

factor in the radar underestimation of the motions. This follows from the unlikelihood that vertical motions would just happen to be in the direction with respect to the radar to cancel out any horizontal shifts.

The GPS sites, particularly the dual-frequency sites, in fact yield vertical components to the displacement. The rms vertical displacement for the GPS sites is 17.2 cm, but most of this is associated with site 7000; when this site is removed, the remaining rms displacement is only 5.1 cm. Ignoring vertical displacements, as was done in our analysis, results in a misinterpretation of lateral shift of magnitude equal to the true vertical movement divided by the tangent of the incidence angle. The errors in the above cases then become 40.5 cm and 12.0 cm, respectively. However, we must note that for nine of the 10 sites the $1 - \sigma$ error in the vertical displacement is larger than that of the measurement itself, so these data must not be overly interpreted.

The second cause for disagreement is error in the measurements. As discussed above, the radar data exhibit statistical errors less than 1 cm rms on both small and medium scales and thus would be insignificant for this comparison. However, large-scale warping of the radar image remains a possibility. We were able to remove most of these effects by minimizing the errors with the least squares removal of planar tilts as described previously. That this correction was approximately correct may be verified by examining the residual motion in the upper and left hand portions of the radar image, those portions farthest from the fault. The observed motion here is very small, as we would expect. If the ERS 1 coverage had been such that the fault was positioned in the center of the radar swath, we could have verified the lack of displacement more accurately all the way around the image. The possibility of a long-scale error thus still exists and may to some degree explain the observed spatial correlation of the errors.

The errors in the GPS/EDM data themselves account for part of the disagreement. The 18 sites listed in Table 2 exhibit an rms error of 9.1 cm in the Stanford analysis, while the 10 GPS-only sites have a 7.7-cm rms error of J. W. Hudnut et al. (personal communication, 1993).

A third possibility is the existence of phase unwrapping errors in the radar data. As each unwrap error results in a one cycle phase error in one interferogram, these errors would appear as $\lambda/2$ errors in $\Delta\rho$, or 8 cm in horizontal shift if it occurred in the April–August pair or 2 cm in the July–August pair. However, we have examined the data for signs of unwrapping errors and believe that the regions near the GPS sites are unwrapped correctly. In addition, it is unlikely again that phase unwrapping mistakes would nearly correct for GPS-observed displacements.

Finally, the locations of the GPS sites are known only to a few tens of meters in the radar image as the radar data are not accurately geocoded, thus leading to estimates at the wrong places. However, we have analyzed the regions around the sites in the radar data and have determined that the displacement does not change rapidly in those areas. Thus even a slight positional shift would not result in a significant error.

Discussion

We have shown that it is possible to map a coseismic displacement field resulting from a major earthquake using only data acquired from an orbiting high-resolution radar system and to achieve results comparable in magnitude to those obtained by conventional field survey techniques. Data from the ERS 1 synthetic aperture radar instrument acquired at three separate instances of time are sufficient to generate a high-resolution, wide area map of the displacements. Comparison of these data with GPS and EDM survey data indicates a high degree of confidence in the radar measurements. We are confident that the differences between the radar and GPS measurements are reconcilable and do not point to a fundamental limitation in the radar technique. Further work is needed along these lines however.

The power of the differential interferometry technique for seismological applications lies in its centimeter-scale measurement sensitivity of line of site displacements over a wide area. The derived displacement fields can be used as a tight constraint in the modeling of earthquake motion. The fine accuracy, fine spatial resolution, and large areal coverage will likely allow increasingly detailed models to be explored, on both large and small spatial scales. The promise of a system to map small-scale fractures in the Earth's surface over a wide region automatically with a remote sensing system will greatly facilitate field activities by permitting concentration in the most important areas.

What of earthquake prediction? Current understanding of the behavior of earthquakes suggests that differential interferometry may not have the accuracy required to detect precursory seismic motions necessary for prediction. Calculations based on theoretical seismic deformation models show small but steady deformation rates in fault zones with a change in the rates occurring within a period of months to years prior to a seismic event [*Lorenzetti and Tullis*, 1989; *Stuart et al.*, 1985]. While the steady deformations have been observed and are well studied, no precursory rate changes have been measured. Furthermore, the steady rates themselves are probably at or below the limits of detectability by differential interferometry, perhaps 10 mm/yr, while the precursory signal is expected to be smaller. Wide area mapping of the surface distribution of these small deformation rates afforded by differential interferometry may provide new insights into local accumulation of strain close to and along a fault, but the possibility that radar interferometry can be used as a predictive tool now appears to be remote. This is not to say that likely future technological advances in spaceborne radar such as higher-resolution, increased signal to noise ratio, and multiple frequency operation will not close this gap and permit the sensitivities required for millimeter-level surface characterization. Nonetheless, in addition to after the fact seismic event modeling, currently radar interferometry can aid in monitoring, forecasting, and in some cases predicting a range of hazardous events. For example, volcanoes are known to bulge prior to eruption at a scale suitable for radar interferometry.

In the short run, existing and planned radar missions such NASA's Shuttle Imaging Radar, the European Space Agency's ERS 2, Canada's Radarsat, and the Japanese JERS 1 system could be operated to emphasize repeat-pass observations at the largest acceptable incidence angles, providing a very large suite of instruments collecting data that may be processed for change detection analysis. For the future one can envision a global seismic satellite mission designed to detect and forecast earthquakes and other natural hazards: a single satellite in a short repeat period orbit similar in design to that proposed by H. A. Zebker et al. (personal communication, 1993) for global topographic mapping. The repeat cycle of the orbit should be short, of the order of 1 day, to minimize the effects of temporal decorrelation. Precise satellite ephemeris from GPS measurements can ensure automatic construction of interferograms and displacement fields. Only three repeat periods of data need to be stored at any time; the processing can proceed in real time, and results can be perused automatically for evidence of anomalous displacements. Detailed design of the radar system and orbital scenario plus the establishment of detection and false alarm thresholds, must await interest by the global community. Given the enormous cost in lives and resources inflicted by earthquakes, interest is sure to follow any evidence that radar interferometry can be used predictively in assessing natural hazards such as earthquakes.

Appendix: Baseline-Induced Displacement Errors

Equation (13) is the displacement determined from the flattened interferometric phase assuming perfect knowledge of the baselines. Reiterating,

$$\Delta\rho = \frac{\lambda}{4\pi}\,[\phi'_{\text{flat}} - \gamma\phi_{\text{flat}}], \tag{A1}$$

where

$$\frac{\lambda}{4\pi}\,\phi_{\text{flat}} = B\,\sin\,(\theta - \alpha) - B\,\sin\,(\theta_0 - \alpha), \tag{A2}$$

$$\gamma = \frac{B'\,\cos\,(\theta_0 - \alpha')}{B\,\cos\,(\theta_0 - \alpha)}. \tag{A3}$$

With imperfect knowledge of the baselines $\hat{B}$ and $\hat{\alpha}$, errors are introduced in both the phase, denoted $\hat{\phi}_{\text{flat}}$, and the scale factor, denoted $\hat{\gamma}$. Defining

$$\hat{B} = B + \delta B \tag{A4}$$

$$\hat{\alpha} = \alpha + \delta\alpha, \tag{A5}$$

we have to first order

$$\frac{\lambda}{4\pi}\,\hat{\phi}_{\text{flat}} = B\,\sin\,(\theta - \alpha) - \hat{B}\,\sin\,(\theta_0 - \hat{\alpha}) = \frac{\lambda}{4\pi}\,\phi_{\text{flat}} - \delta B\,\sin\,(\theta - \alpha) - \delta\alpha B\,\cos\,(\theta_0 - \alpha) \tag{A6}$$

and

$$\hat{\gamma} = \frac{\hat{B}'\,\cos\,(\theta_0 - \hat{\alpha}')}{\hat{B}\,\cos\,(\theta_0 - \hat{\alpha})} = \frac{B'\cos(\theta_0 - \alpha') + \delta B'\cos(\theta_0 - \alpha') + \delta\alpha' B'\sin(\theta_0 - \alpha')}{B\cos(\theta_0 - \alpha) + \delta B\cos(\theta_0 - \alpha) + \delta\alpha B\sin(\theta_0 - \alpha)}. \tag{A7}$$

Note that for $\hat{\gamma}$, baseline length error and angle error are complementary: baseline length error is weighted highly when the baseline is orthogonal to the look direction ($\theta_0 - \alpha_i = 0$), whereas angle error is weighted highly with the baseline aligned with the look direction. For baselines that are not nearly aligned with the look direction, the ratio in (A7) may be expanded to give

$$\hat{\gamma} = \gamma\left[1 + \frac{\delta B'}{B'} - \frac{\delta B}{B} + \delta\alpha'\,\tan\,(\theta_0 - \alpha') - \delta\alpha\,\tan\,(\theta_0 - \alpha)\right]. \tag{A8}$$

Using (A6) and (A8) to evaluate the displacement gives

$$\begin{aligned}\Delta\hat{\rho} &= \frac{\lambda}{4\pi}\,[\hat{\phi}'_{\text{flat}} - \hat{\gamma}\hat{\phi}_{\text{flat}}]\\ &= \Delta\rho - \delta B'\,\sin\,(\theta_0 - \alpha') + \delta\alpha' B'\,\cos\,(\theta_0 - \alpha')\\ &\quad - \gamma[-\delta B'\,\sin\,(\theta_0 - \alpha') + \delta\alpha' B'\,\cos\,(\theta_0 - \alpha')]\\ &\quad - \gamma\,\frac{\lambda}{4\pi}\,\phi_{\text{flat}}\left[\frac{\delta B'}{B'} - \frac{\delta B}{B} + \delta\alpha'\,\tan\,(\theta_0 - \alpha') - \delta\alpha\,\tan\,(\theta_0 - \alpha)\right]\end{aligned} \tag{A9}$$

Equation (A9) shows that in addition to the desired term $\Delta\rho$, there are slowly varying (fraction of a cycle) sinusoidal artifacts across the displacement field and topographic residuals dependent on baseline length and angle errors. Even if the slowly varying artifacts are removed empirically, accurate estimates of the displacements, to fractions of a cycle, require fairly accurate baseline knowledge. We can estimate the scale of the topographic term as follows. Assume $B \approx B'$ and likewise for the uncertainties δB and $\delta\alpha$. Then the final term in (A9) becomes

$$\Delta\hat{\rho}_{\text{topo}} \sim \frac{\lambda}{4\pi}\,\phi_{\text{flat}}\,\frac{\delta B_{\text{net}}}{B_{\text{net}}} \tag{A10}$$

where we have assumed a worse case $\gamma = 1$ and an equivalent net baseline error δB_{net} including δB and $\delta\alpha B$. Expanding $\phi_{\text{flat}}(\theta)$ about θ_0,

$$\Delta\hat{\rho}_{\text{topo}} \sim \delta B_{\text{net}}\delta\theta,$$

where $\delta\theta = z/\rho$ is the angular deviation of the look direction due to topography. Thus, to limit displacement errors due to residual topography, $\Delta\hat{\rho}_{\text{topo}}$, to say 1/4 wavelength, the error in δB_{net} must satisfy the inequality

$$\delta B_{\text{net}} < 0.25\lambda\rho/z_{\max}$$

where $z_{\max}$ is the maximum topographic extent over the scene. For $\rho = 800{,}000$ m, $\lambda = 0.0566$ m, $z_{\max} = 5000$ m, $\delta B_{\text{net}} < 2.3$ m.

Acknowledgments. We would like to acknowledge Paul Segall for supplying the GPS/EDM measurements and for several useful discussions regarding the intercomparison of the data sets. We would also like to acknowledge discussions with Ken Hudnut for discussions prompting a reexamination of the comparison of our results with the GPS/EDM data. The research described in this paper was carried out by the Jet Propulsion Laboratory, California Institute of Technology, under a contract with the National Aeronautics and Space Administration.

References

Curlander, J. C., and R. N. McDonough, *Synthetic Aperture Radar*, Wiley-Interscience, New York, 1991.

Elachi, C., *Spaceborne Radar Remote Sensing: Applications and Techniques*, IEEE Press, New York, 1987.

Evans, D. L., T. G. Farr, H. A. Zebker, J. J. van Zyl, and P. J. Mouginis-Mark, Radar interferometric studies of the Earth's topography, *Eos Trans. AGU*, *73*, 553, 557–558, 1992.

Gabriel, A. G., R. M. Goldstein, and H. A. Zebker, Mapping small elevation changes over large areas: Differential radar interferometry, *J. Geophys. Res.*, *94*, 9183–9191, 1989.

Ghiglia, D. C., and L. Romero, Robust two-dimensional weighted and unweighted phase unwrapping using fast transforms and iterative methods, *J. Opt. Soc. Am.*, *11*, 107–117, 1993.

Goldstein, R. M., and H. A. Zebker, Interferometric radar measurement of ocean surface currents, *Nature*, *328*, 707–709, 1987.

Goldstein, R. M., H. A. Zebker, and C. L. Werner, Satellite radar interferometry: two dimensional phase unwrapping, *Radio Sci.*, *23*, 713–720, 1988.

Goldstein, R. M., T. P. Barnett, and H. A. Zebker, Remote sensing of ocean currents, *Science*, *246*, 1282–1285, 1989.

Gray, A. Laurence, and P. J. Farris-Manning, Two-pass interferometry with airborne synthetic aperture radar, *IEEE Trans. Geosci. Remote Sens.*, *31*, 180–191, 1993.

Li, F., and R. M. Goldstein, Studies of multi-baseline spaceborne interferometric synthetic aperture radars, *IEEE Trans. Geosci. Remote Sens.*, *28*, 88–97, 1990.

Lorenzetti, E., and T. E. Tullis, Geodetic predictions of a strike-slip fault model: Implications for intermediate and short-term earthquake prediction, *J. Geophys. Res.*, *94*, 12,343–12,361, 1989.

Madsen, S. N., H. A. Zebker, and J. Martin, Topographic mapping using radar interferometry: Processing techniques, *IEEE Trans. Geosci. Remote Sens.*, *31*, 246–256, 1993.

Massonnet, D., M. Rossi, C. Carmona, F. Adragna, G. Peltzer, K. Feigl, and T. Rabaute, The displacement field of the Landers earthquake mapped by radar interferometry, *Nature*, *364*, 138–142, 1993.

Prati, C., F. Rocca, A. Monti Guarnieri, and E. Damonti, Seismic migration for SAR focusing: Interferometrical applications, *IEEE Trans. Geosci. Rem. Sens.*, *28*, 627–640, 1990.

Stuart, W. D., R. J. Archuleta, and A. G. Lindh, Forecast model for moderate earthquakes near Parkfield, California, *J. Geophys. Res.*, *90*, 592–604, 1985.

Zebker, H. A., and R. M. Goldstein, Topographic mapping derived from synthetic aperture radar measurements, *J. Geophys. Res.*, *91*, 4993–4999, 1986.

Zebker, H. A., and J. Villasenor, Decorrelation in interferometric radar echoes, *IEEE Trans. Geosci. Remote Sens.*, *30*, 950–959, 1992.

Zebker, H. A., S. N. Madsen, J. Martin, K. B. Wheeler, T. Miller, Y. Lou, G. Alberti, S. Vetrella, and A. Cucci, The TOPSAR interferometric radar topographic mapping instrument, *IEEE Trans. Geosci. Rem. Sens.*, *30*, 933–940, 1992.

A. Gabriel, R. M. Goldstein, P. Rosen, C. L. Werner, and H. A. Zebker, MS 300-227, Jet Propulsion Laboratory, 4800 Oak Grove Drive, Pasadena, CA 91109.

(Received December 6, 1993; revised April 21, 1994; accepted April 29, 1994.)